

Is Bigger Always Better? Efficiency Analysis in Resource-Constrained Small Object Detection

Kwame Mbobda-Kuate

ENSAE Paris

5 avenue Henry Le Chatelier,
91120 Palaiseau

{firstname.lastname}@ensae.fr

Gabriel Kasmi

Centre O.I.E., Mines Paris - PSL University

1 Rue Claude Daunesse,
06904 Sophia-Antipolis

{firstname.lastname}@minesparis.psl.eu

Abstract

Scaling laws assume larger models trained on more data consistently outperform smaller ones — an assumption that drives model selection in computer vision but remains untested in resource-constrained Earth observation (EO). We conduct a systematic efficiency analysis across three scaling dimensions: model size, dataset size, and input resolution, on rooftop PV detection in Madagascar. Optimizing for model efficiency (mAP_{50} per unit of model size), we find a consistent efficiency inversion: YOLO11N achieves both the highest efficiency ($24\times$ higher than YOLO11X) and the highest absolute mAP_{50} (0.617). Resolution is the dominant resource allocation lever ($+120\%$ efficiency gain), while additional data yields negligible returns at low resolution. These findings are robust to the deployment objective: small high-resolution configurations are Pareto-dominant across all 44 setups in the joint accuracy–throughput space, leaving no tradeoff to resolve. In data-scarce EO, bigger is not just unnecessary: it can be worse.

1. Introduction

Deep learning progress in computer vision has been largely driven by scaling: larger models trained on larger datasets consistently push benchmark performance upward. This paradigm, formalized through scaling laws [12, 15], has proven remarkably predictable in data-rich settings such as NLP and large-scale image classification [7, 40]. The implicit assumption that more parameters and more data always help has become the default prior for model selection in computer vision.

Earth observation (EO) challenges this assumption on two fronts. First, EO datasets are structurally data-scarce: annotation is expensive, requires domain expertise, and is geographically uneven [6]. Second, deployment in opera-

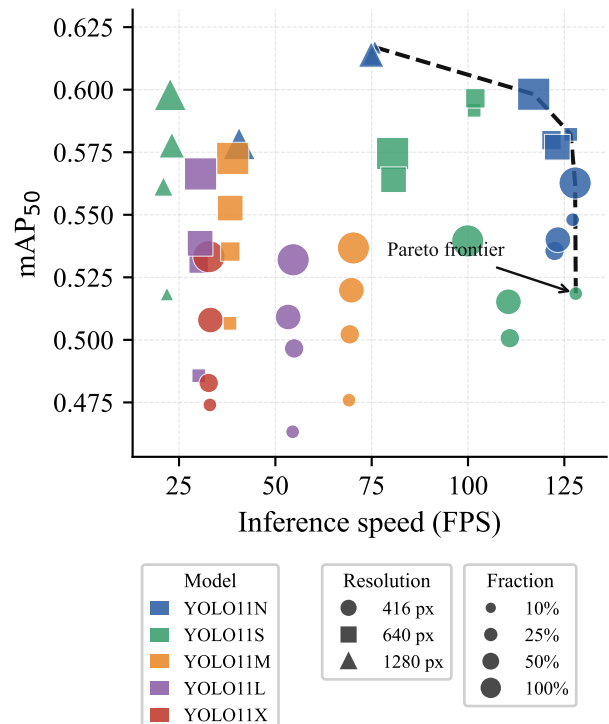


Figure 1. **Small models at high resolution dominate across all deployment objectives.** Detection performance (mAP_{50}) versus inference speed (FPS) for all 44 experimental configurations on the OpenStat Madagascar rooftop PV dataset [27]. Marker shape encodes input resolution (circle: 416 px, square: 640 px, triangle: 1280 px) and marker size encodes the training dataset fraction (10% to 100%). The dashed line delineates the Pareto frontier (the set of configurations for which no other configuration is superior on both axes simultaneously). YOLO11N and YOLO11S at 1280 px lie at the apex, simultaneously maximising accuracy and throughput with no accuracy–speed tradeoff to resolve.

tional settings, e.g., in developing countries where most renewable energy growth will occur [13], imposes hard com-

pute constraints that make large models impractical regardless of their accuracy. In this regime, the relevant criterion is not raw performance but *efficiency*: performance per unit of resource.

Despite growing evidence that architectural innovation can match or exceed naive parameter scaling [10, 31, 35], and that smaller models outperform larger ones below certain data thresholds [4], no systematic analysis has jointly characterized the interplay between model size, dataset fraction, and input resolution in a data-scarce EO setting. Existing work addresses these dimensions in isolation — resolution effects [30], data-scarce regimes [4], or budget-aware detection [28] — but their joint optimization under operational constraints remains an open question.

This paper addresses that gap through a systematic efficiency analysis of the YOLO11 [14] model family on rooftop photovoltaic (PV) detection in Madagascar — a representative data-scarce, small object EO task in a developing country context. We evaluate five model variants across four dataset fractions and three input resolutions, defining efficiency as mAP_{50} per unit of model size following [35]. As illustrated in Figure 1, our analysis reveals a striking result: the smallest model (YOLO11N, 2.6M parameters) achieves both the highest absolute mAP_{50} and a $24\times$ efficiency advantage over the largest variant — and lies at the apex of the accuracy–throughput Pareto frontier, directly contradicting the scaling intuition. We further show that resolution dominates data volume as a resource allocation lever, and that this recommendation is robust to the choice of deployment objective: small high-resolution configurations simultaneously maximize detection accuracy and inference throughput, leaving no accuracy–speed tradeoff to resolve. We provide a mechanistic explanation grounded in the bias-variance tradeoff, compute-optimal training theory [12, 36], and the structural absence of domain transfer from large-scale pretraining in this setting.

The key contributions of this work are:

- A systematic efficiency analysis across three scaling dimensions (model size, dataset fraction, input resolution) in a data-scarce EO setting, yielding 44 training runs on a real-world rooftop PV dataset.
- Evidence that smaller models dominate larger ones in both accuracy and efficiency under data scarcity, with a $24\times$ efficiency gap between YOLO11N and YOLO11X.
- A mechanistic explanation of this inversion grounded in overparameterization theory, supported by empirical learning curves and overparameterization ratio analysis.
- A practical resource allocation recommendation: prioritize input resolution over dataset volume, and select the smallest model consistent with task requirements.
- A joint efficiency–throughput analysis showing that small high-resolution configurations are Pareto-dominant across all experimental setups, confirming that the re-

source allocation recommendation holds regardless of whether the practitioner prioritizes static efficiency or real-time deployment.

2. Related works

2.1. Scaling Laws and Model Efficiency

A classical assumption underpinning the scaling paradigm is that larger models consistently outperform smaller ones across domains [15]. This assumption has driven state-of-the-art progress in NLP, where models are trained in a self-supervised manner on colossal amounts of text — a setting fundamentally different from the data-scarce, domain-specific regime we consider. Several lines of work challenge its generality in vision. The lottery ticket hypothesis shows that sparse subnetworks within large models can match full model performance [10], suggesting substantial parameter redundancy. EfficientNet [35] demonstrated that compound scaling outperforms naive parameter scaling and introduced *model efficiency*, i.e., detection performance per unit of model size, as the operationally relevant criterion for resource-constrained deployment, a definition we adopt directly. Vision transformer scaling studies further reveal diminishing returns at larger scales [1], suggesting that the relationship between model size and performance is neither monotonic nor universal.

Two distinct notions of efficiency recur in this literature and are worth distinguishing explicitly. *Model efficiency* (mAP per unit of model size or parameters) captures the static deployment cost — the criterion relevant when memory footprint constrains model selection on edge devices. *Inference throughput* (mAP per unit of inference time, typically visualized as accuracy–FPS Pareto frontiers) captures the dynamic deployment cost — the criterion relevant when latency constrains real-time operation. These two notions are correlated but not equivalent: a model with a small memory footprint may not be the fastest at inference, particularly when input resolution increases GFLOPs independently of parameter count. Most prior work optimizes for one criterion implicitly without acknowledging the other; we address both explicitly and show that, in our setting, the same configurations dominate on both axes simultaneously.

More directly relevant to our setting, Shi et al. [31] show that small vision models augmented with multi-scale features can surpass much larger counterparts on classification and detection tasks in terms of both model efficiency and raw accuracy, questioning the need for large models beyond a certain data regime. Through their Scaling on Scales method, they demonstrate that multi-scale feature augmentation recovers the performance gap between small and large models at a fraction of the parameter cost — a result consistent with our finding that input resolution, rather than model capacity, is the dominant resource allocation

lever in data-scarce settings.

2.2. Small Object Detection in Remote Sensing

Small object detection presents challenges that are orthogonal to model scaling: limited feature representation at low resolutions, high intra-class scale variation, and domain shift between classification pretraining and detection fine-tuning [32]. Aerial and satellite imagery compounds these difficulties through viewpoint variation, occlusion, and background clutter [5]. Architectural responses include feature pyramid networks [25] and multi-scale sampling strategies [33], while context-aware augmentation has been shown to compensate for training sample scarcity [8].

Critically for our setting, resolution scaling has been shown to be more effective than model scaling for small object detection in satellite imagery. Shermeyer and Van Etten [30] demonstrate that increasing input resolution yields substantial gains in aerial object detection performance, despite being done through super-resolution techniques. They find on the test set that performance degrades from mAP = 0.53 at 30 cm resolution, down to mAP = 0.11 at 4.8 m resolution, while super-resolving native 30 cm imagery to 15 cm yields the greatest benefit; a 13 – 36% improvement in mAP.

2.3. Data-Scarce Regimes and Resource-Constrained Learning

Traditional scaling laws assume data abundance, an assumption that breaks down in specialized domains with limited annotation budgets. Few-shot learning addresses this by exploiting architectural priors to generalize from few examples [34], while meta-learning extends this to rapid domain adaptation [9]. Transfer learning offers a complementary strategy, though its effectiveness varies significantly with the domain gap between pretraining and target tasks [38], a limitation directly relevant to our setting, where COCO-pretrained models face an out-of-distribution target domain (see Sec. 9.3).

Beyond architectural solutions, recent work has examined the optimal allocation of a fixed resource budget. Brigato and Iocchi [4] demonstrate empirically that smaller models outperform larger ones below a dataset-size threshold (160 samples per class on CIFAR-10 and Fashion-MNIST, 80 on Street View House Numbers), establishing a crossover regime that directly motivates our analysis. Nonetheless, given that there are no classes in segmentation tasks, the impact of this finding should be put into perspective. Hoffmann et al. [12] formalize compute-optimal training, showing that model size and data volume must scale proportionally for optimal performance (with a token / parameters ratio of 20:1) — a model undertrained relative to its capacity is systematically suboptimal. In the object detection setting specifically, Pardo et al. [28]

introduce Budget-Aware Object Detection (BAOD), showing that jointly optimizing annotation strategy under a fixed budget matches fully-supervised performance while reducing annotation cost by 12.8%. While these authors worked with the same model and varied the image dataset and the annotation scheme, we aim here to explore the first two dimensions and keep the latter fixed. Furthermore, the budget constraint is moved from the training phase to the evaluation one with efficiency metrics.

2.4. Rooftop PV Detection from Satellite Imagery

Rooftop PV detection from satellite imagery is well-established in developed countries, where high-resolution imagery is readily available. Existing works leverage CNN and ViT-based architectures across France [17], Germany [26], the Netherlands [20], and the United States [39]. These works primarily optimize for accuracy under data abundance, with only limited attention to inference and deployment cost [16, 29].

Developing countries have received comparatively little attention, despite cumulating high solar potential and operating less resilient electric grids where unmonitored PV installations carry greater grid stability risks [13]. PV mapping in these contexts remains largely unexplored, with only isolated case studies in Tunisia [2]. This gap motivates our choice of the OpenStat Madagascar dataset [27]: it provides a realistic data-scarce benchmark with limited annotation budgets, heterogeneous imagery, and deployment under compute constraints — a natural testbed for our efficiency analysis.

The works reviewed above address complementary dimensions of the efficiency problem, but always in isolation: scaling laws [12, 15] operate in data-abundant NLP settings; data-scarce regime studies [4] focus on image classification rather than detection; budget-aware detection [28] treats model size as fixed; and resolution studies [30] vary input resolution independently of model complexity and data volume. No existing work jointly characterizes the interplay between model size, dataset fraction, and input resolution in a data-scarce Earth observation setting, leaving practitioners with no principled guidance on how to allocate a fixed resource budget across these three dimensions simultaneously. This paper addresses that gap.

3. Methods

Our aim is to systematically investigate the effects of model size, input resolution, and training dataset size on detection performance under resource constraints. Specifically, we address the following research question: *given a fixed resource budget, what is the optimal allocation between model complexity, data volume, and image resolution for small object detection in a data-scarce Earth observation setting?* Throughout our experiments, we report computa-

tional cost alongside accuracy metrics, and define our measure of interest as efficiency rather than pure performance.

We focus on efficiency rather than pure accuracy because, in resource-constrained deployment contexts, a model that achieves marginally higher detection performance at disproportionate computational cost is not operationally viable. Efficiency captures performance per unit of resource — the relevant criterion for practitioners operating under hardware constraints, a setting representative of Earth observation applications in developing countries.

3.1. Experimental Setup

We conduct systematic scaling experiments across three dimensions: model complexity, dataset fraction, and input resolution, producing a factorial grid of training configurations.

Model Complexity. We evaluate five YOLO11 [14] variants with increasing capacity, spanning a $22\times$ range in parameter count and a $21\times$ range in model size:

Table 1. YOLO11 model variants evaluated in this study.

Variant	Parameters	Size (MB)
YOLO11N	2.6M	5.1
YOLO11S	9.5M	18.1
YOLO11M	20.1M	38.4
YOLO11L	25.4M	48.5
YOLO11X	57.0M	108.6

Dataset Fraction. Each model is trained on four fractions of the available training set: 10% (897 images), 25% (2,244 images), 50% (4,488 images), and 100% (8,977 images). This design allows us to characterize model behavior across a realistic range of annotation budgets, from severely data-scarce to fully supervised.

Input Resolution. We evaluate three input resolutions: 416 px, 640 px, and 1280 px. Resolution directly affects the visibility of small rooftop PV installations and constitutes an independent axis of the resource budget as higher resolution increases both GPU memory consumption and inference time.

Training Grid. These settings produce $5 \times 4 \times 3 = 60$ nominal combinations. Due to GPU memory constraints (NVIDIA A2, 16GB), the most demanding configurations (large models at 1280 px) are excluded, yielding a total of 44 completed training runs. Table 3 in Appendix 8 illustrates the full configuration space with missing entries indicated.

Hyperparameters. All runs share identical hyperparameters to ensure fair comparison: 50 epochs, data augmentations, batch size 32 (reduced to 8 at 1280 px due to memory constraints), Adam optimizer with learning rate 10^{-3} , and a fixed random seed. All models are initialized from COCO-pretrained weights.

3.2. Evaluation Metrics

Following [35], we define model efficiency as the ratio of detection performance to model size:

$$\text{Eff} = 10 \times \frac{\text{mAP}_{50}}{\text{ModelSize (MB)}}$$

Higher values indicate better performance per unit of storage cost. The scaling factor of 10 is chosen so that the efficiency score is interpretable around unity: a model achieving $\text{mAP}_{50} = 0.5$ with a 5 MB footprint yields $\text{Eff} = 1.0$, providing a natural break-even reference. We adopt model size (MB) rather than FLOPs as the denominator for two reasons: (1) model size is a fixed, resolution-independent quantity, whereas FLOPs vary with input resolution and would confound the experimental design; (2) model size directly captures deployment cost in memory-constrained edge environments.

We acknowledge that model size is an imperfect proxy for computational cost: a model twice as large does not necessarily require twice the inference time. However, our conclusions are robust to this choice: Sec. 5.4 independently confirms the same ranking using a throughput-based criterion (FPS), and Sec. 9.1 shows that the efficiency ordering is invariant to the choice of numerator metric. Secondary metrics including mAP_{50-95} , precision, and recall are reported in Sec. 9.1 for completeness.

4. Data

4.1. OpenStat Madagascar Dataset

The OpenStat Madagascar dataset [27] is a crowdsourced collection of annotated imagery of rooftop photovoltaic installations across Madagascar, curated by the Madagascar Initiatives for Digital Innovation (MAIDI) with support from the Lacuna Fund. Images were acquired between July and September 2023 through two modalities: satellite screenshots captured via Google Earth ($\simeq 700 \times 400$ px) and drone imagery (ranging from 3840×2160 px to 5280×3956 px). The annotation methodology combined visual identification on satellite imagery with 25% ground-truth field verification, followed by manual polygon annotation of individual solar objects using GIMP. The full dataset contains 130,500 annotated solar objects across 11,154 images corresponding to 8,454 distinct geolocations. Object types include rooftop solar panels (85.5%), solar boilers (10.5%), mixed installations (3.8%), and solar parks ($<0.1\%$).

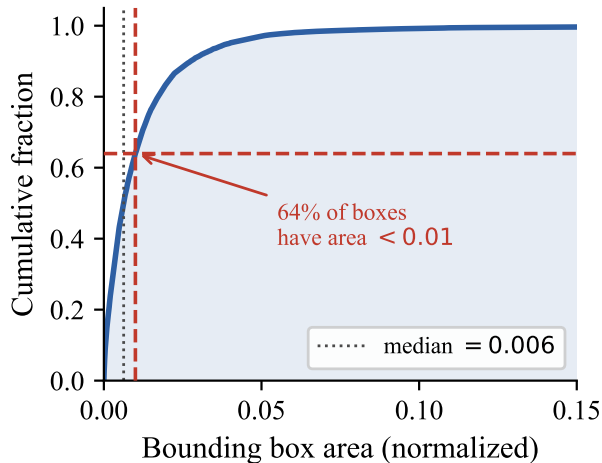


Figure 2. **Cumulative distribution of bounding box areas (normalized by image area) across the training set.** The median normalized area is 0.006, and 64% of boxes fall below the 0.01 threshold commonly used to define small objects in detection benchmarks [25]. This confirms that rooftop PV detection in drone imagery is structurally a small object task, justifying the central role of input resolution in our efficiency analysis.

This dataset fills a notable gap in the PV detection literature. Existing labeled datasets cover France [18] or the United States [3, 11], and worldwide coverage [21, 23] is limited to PV plants. These datasets rely on satellite or aerial imagery at fixed resolution, with annotations collected under controlled conditions and expert supervision. OpenStat Madagascar is, to our knowledge, the first large-scale PV detection dataset based predominantly on drone imagery (90% of images), providing substantially higher spatial resolution than satellite-based counterparts. As shown in Figure 2, 64% of annotated bounding boxes have a normalized area below 0.01, confirming the small object nature of the detection task and directly motivating our focus on resolution as a resource allocation lever.

4.2. Dataset Construction and Splits

For model training, we restrict the dataset to drone images and exclude images containing no solar panels, reducing the dataset from 11,154 to 8,977 images. Satellite images are excluded due to their substantially lower resolution, which would conflate resolution effects with modality effects in our scaling analysis. We convert polygon annotations to axis-aligned bounding boxes for compatibility with YOLO11. Among the retained images, 8,832 (98.4%) contain only rooftop solar panels and 145 (1.6%) contain both solar panels and boilers.

The dataset is split randomly into training (80%, 7,181 images), validation (10%, 899 images), and test (10%, 897 images) sets. Stratified sampling ensures class balance

is preserved across splits. The geographic distribution of images across splits is presented in Appendix 7, Fig. 7: sampling points are concentrated along major transportation corridors and around Antananarivo, with secondary clusters along the east coast and in the southern regions around Fianarantsoa and Toliara. Annotations were produced through crowdsourcing rather than expert labeling, imagery sources and acquisition conditions are heterogeneous, and geographic coverage reflects access constraints rather than systematic sampling — making this a realistic, if challenging, benchmark representative of the data quality faced by practitioners in developing countries. The random split does not enforce spatial disjointness, which may introduce an optimistic bias in absolute mAP_{50} values; however, since this bias affects all model variants equally, relative efficiency rankings are unaffected.

5. Results

5.1. Model Size: Smaller is Better

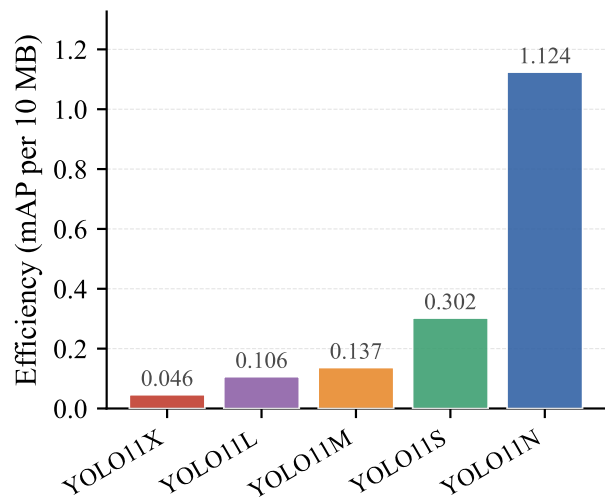


Figure 3. **Efficiency ranking of the evaluated models (mAP per 10 MB).** YOLO11N achieves 24× higher efficiency than YOLO11X while also reaching the highest absolute mAP_{50} — ruling out any accuracy–efficiency tradeoff.

Figure 3 reports efficiency statistics across all YOLO11 variants. YOLO11N achieves the highest average efficiency (1.124) and the highest absolute mAP_{50} (0.617) simultaneously (see Table 4 in Appendix 8), ruling out the hypothesis that larger models compensate their resource cost through superior detection performance. Its 21× larger footprint makes YOLO11X’s efficiency 24× lower. Across all variants, the efficiency spread within a given model remains modest (11–19%), confirming that architecture choice dominates over configuration choice. Robustness checks in the

appendix confirm this result across alternative efficiency measures (Sec. 9.1) and at fixed configurations (Sec. 9.2).

5.2. Why Small Models Outperform: The Data-Scarce Regime Penalizes Large Models

On large benchmarks (COCO [24], DOTA [37], xView [22]), larger models consistently dominate when data is abundant. We argue this intuition breaks down here, and provide two complementary pieces of evidence.

Large models depend on data volume they do not have.

Figure 4 shows data efficiency curves averaged across input resolutions. YOLO11N starts high and remains stable: its performance at 10% of the training data ($mAP_{50} = 0.582$) is virtually identical to its performance at 100% (-0.5% relative change). By contrast, YOLO11X and YOLO11L start at $mAP_{50} = 0.474$ and require the full dataset to approach competitive performance ($+12.5\%$ and $+15.7\%$ respectively). Relative gains increase monotonically with model size (YOLO11S: $+5.3\%$, YOLO11M: $+12.9\%$), confirming that larger models are structurally more data-hungry.

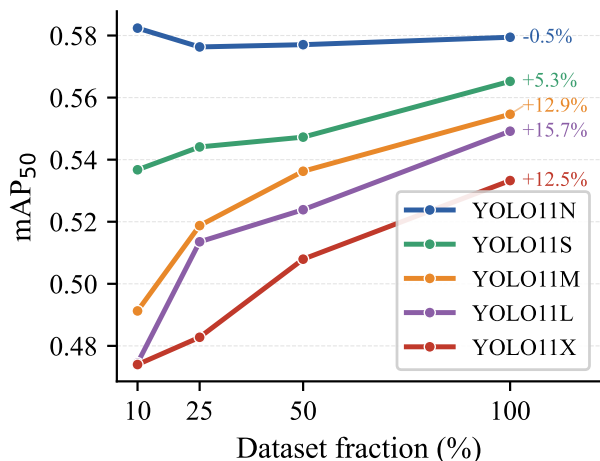


Figure 4. **Data efficiency curves for each YOLO11 variant averaged across input resolutions.** YOLO11N shows near-zero sensitivity to data volume (-0.5% from 10% to 100%), while larger models exhibit pronounced data hunger. Relative gains increase monotonically with model size.

Overparameterization penalizes generalization.

Figure 5 plots mAP_{50} against the overparameterization ratio $\rho = \text{params}/N_{\text{train}}$, ranging from ~ 300 (YOLO11N, 100% data) to $\sim 80,000$ (YOLO11X, 10% data). A clear negative log-linear trend emerges, consistent with the classical bias-variance tradeoff [36]: excess capacity leads to memorization rather than generalization. This effect is compounded

by the structural absence of COCO domain transfer — zero-shot evaluation yields $mAP_{50} \leq 0.004$ across all configurations (Sec. 9.3), confirming that pretrained representations provide no exploitable prior for this task.

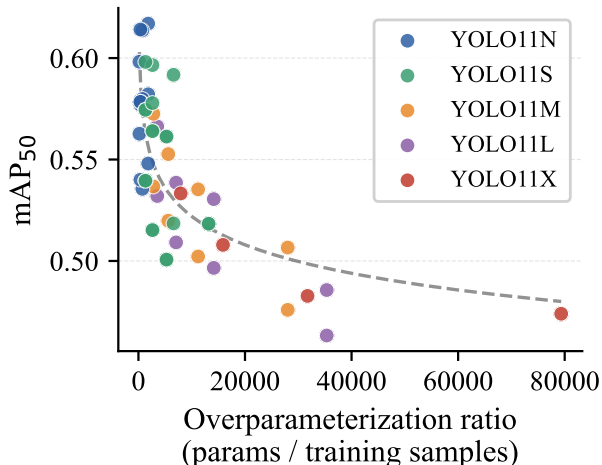


Figure 5. **mAP_{50} vs. overparameterization ratio $\rho = \text{params}/N_{\text{train}}$.** A negative log-linear trend confirms that higher overparameterization predicts lower performance, consistent with the bias-variance tradeoff. Each point is one configuration (model \times fraction \times resolution).

Theoretical grounding.

These observations are consistent with three convergent lines of work. Vapnik [36] establishes that generalization error grows with model capacity relative to training set size and our ρ curve provides a direct empirical instantiation of this bound. Brigato and Iocchi [4] confirm that smaller models outperform larger ones below a dataset-size threshold, with a crossover in precisely the low-data regime we study. Hoffmann et al. [12] show that model size and data volume must scale proportionally for optimal performance, with a 20:1 token-to-parameter ratio for compute-optimal training. Approximating tokens as non-overlapping 16×16 image patches, our training set yields $\sim 57\text{M}$ tokens, placing YOLO11N (2.6M parameters) near the compute-optimal regime, while YOLO11X (57M parameters) operates at a $20\times$ deficit. This provides a principled explanation for the efficiency inversion: only the smallest model is trained in a regime where its capacity is matched to the available data.

5.3. Resource Allocation: Resolution or Data First?

Having established that model size should be minimized, we now ask: given a fixed budget, should practitioners prioritize more data or higher resolution?

Table 2 reports average relative efficiency normalized by the baseline (416 px, 10%). Three findings stand out. First,

at 416 px, efficiency remains flat regardless of data volume (1.00–1.05): additional annotation yields negligible gains at low resolution. Second, resolution dominates: moving to 640 px yields $\sim 30\%$ gain; 1280 px exceeds 120% even at 10% data. Third, resolution and data volume operate largely independently — at 1280 px, efficiency peaks at 50% data (2.28) and reverses beyond it (2.19). The recommendation is clear: **invest in resolution first, then in data volume**.

Table 2. Average relative efficiency normalized by baseline (416 px, 10%). Best per resolution in bold.

Resolution	10%	25%	50%	100%
416 px	1.00	0.99	1.00	1.05
640 px	1.30	1.31	1.30	1.35
1280 px	2.24	2.27	2.28	2.19

Finally, the efficiency ratio between YOLO11N and larger variants remains stable at $\approx 2.2\times$ across all resolutions (Sec. 9.4), confirming that resolution and model size operate on orthogonal axes. Since COCO pretraining provides no exploitable prior (Sec. 9.3), resolution becomes the sole architectural lever to access discriminative features, making it not merely beneficial but structurally necessary.

Figure 6 illustrates why resolution matters. At 416 px, aliasing artefacts affect the fine-grained texture and edge detail characteristic of PV modules. Higher resolutions progressively restore these high-frequency components, consistent with [19], who show that high-frequency features are disproportionately fragile under distribution shifts including GSD variations. When altered by downscaling, the model loses access to the discriminative features that make PV panels identifiable.

5.4. Joint Efficiency–Throughput Tradeoff

Figure 1 plots mAP_{50} against inference speed (FPS) across all 44 configurations. YOLO11N and YOLO11S at 1280 px jointly dominate the Pareto frontier, simultaneously maximizing accuracy and throughput, outperforming heavier architectures at standard resolution. Small high-resolution models thus dominate on both static efficiency (Sections 5.1, 5.3) and dynamic throughput, leaving no tradeoff to resolve. The practical recommendation is unambiguous: scale resolution, not model size.

6. Conclusion and future works

6.1. Summary of Findings

This paper investigated the efficiency of YOLO11 model variants across three resource dimensions (model size, dataset fraction, and input resolution) for rooftop PV detection in a data-scarce Earth observation setting. Three findings emerge consistently from our analysis.

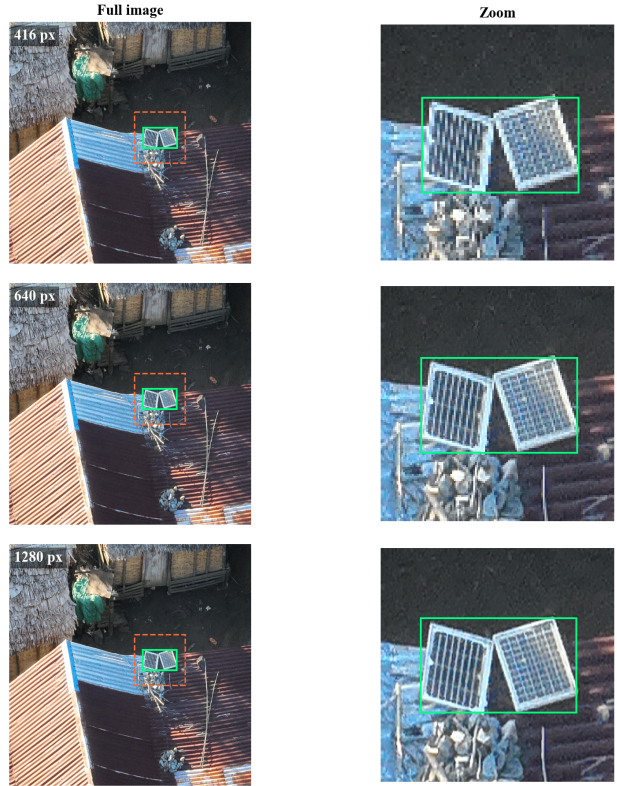


Figure 6. Effect of input resolution on visual information for PV detection. Same scene at 416 px (top), 640 px (middle), 1280 px (bottom). Right column: zoomed crop at fixed physical size. At 416 px the panel texture is aliased and geometrically ambiguous; at 1280 px cell structure and edges are clearly resolved.

First, smaller models dominate and the data-scarce regime explains why. YOLO11N achieves both the highest absolute mAP_{50} (0.617) and a $24\times$ efficiency advantage over YOLO11X. This inversion is not accidental: data efficiency curves reveal that YOLO11N reaches near-peak performance at 10% of the training data (-0.5% relative change at 100%), while the overparameterization ratio $\rho = \text{params}/N_{\text{train}}$ negatively predicts mAP_{50} across all configurations — consistent with the bias-variance tradeoff and the absence of useful COCO domain transfer.

Second, resolution is the dominant resource allocation lever. At fixed resolution (416px), increasing dataset fraction from 10% to 100% yields a $1.05\times$ efficiency gain. Moving from 416px to 1280px at 50% data yields $2.28\times$. The practical recommendation is unambiguous: **invest in resolution first, then in data volume, and select the smallest model consistent with task requirements**.

Third, these findings are robust to the choice of deployment objective. The joint efficiency–throughput analysis (Figure 1) confirms that small high-resolution configurations are not only statically efficient but also operationally

dominant: YOLO11N and YOLO11S trained at 1280 px lie at the apex of the Pareto frontier across all 44 configurations, simultaneously maximising detection accuracy and inference speed. No accuracy–throughput tradeoff needs to be resolved as the same configurations that minimize model size and maximize resolution are optimal regardless of whether the practitioner prioritizes static efficiency or real-time deployment.

6.2. Limitations

Several limitations bound the generalizability of our conclusions. First, our analysis is restricted to the YOLO11 single-stage detector family; transformer-based architectures and two-stage detectors exhibit different capacity-efficiency tradeoffs and may not display the same efficiency inversion under data scarcity. Second, our analysis does not include comparison with methods specifically designed for small object detection — such as super-resolution preprocessing or scale-aware training strategies [30, 33] — which may interact differently with model size and resolution scaling; whether the efficiency inversion holds when such methods are applied remains an open question. Third, all conclusions are drawn from a single geographic context and object type (Madagascar rooftop PV); generalization to other EO detection tasks should be validated empirically before the resource allocation recommendations are applied unconditionally. Fourth, our resolution range (416–1280px) is constrained by available GPU memory; higher resolutions may reveal different scaling patterns, particularly for very small objects. Finally, our conclusions are conditioned on COCO initialization, which provides no exploitable prior for this task; a stronger initialization — such as domain-adaptive or self-supervised pretraining on EO imagery — may shift the crossover point between model sizes and alter the observed scaling behavior.

6.3. Future Work

Three directions extend this work naturally. First, validating our findings across diverse model families — vision transformers, EfficientNet variants — would establish whether the efficiency inversion is architecture-specific or a general property of the data-scarce regime. Second, formalizing efficiency-based scaling laws for resource-constrained EO settings would allow predictive resource allocation, moving from empirical observation to theoretical guidance. Third, real-world deployment studies measuring operational efficiency on edge devices would close the loop between our training-time analysis and the inference constraints faced by practitioners in developing countries. A related direction is the evaluation of domain-adaptive pretraining strategies such as self-supervised pretraining on unlabeled EO imagery, which may reduce the domain gap and, by providing a stronger initialization, alter the relative advantage

of small models observed here. Finally, our dataset split follows a random rather than geographically stratified strategy, which may introduce spatial autocorrelation between train and test sets. Replacing the random split with a tile-based spatial split — ensuring geographic disjointness between partitions — would provide a stricter evaluation of generalization and yield a more conservative, deployment-realistic estimate of the efficiency gains reported here.

References

- [1] Lucas Beyer, Xiaohua Zhai, and Alexander Kolesnikov. Better plain ViT baselines for ImageNet-1k, 2022. 2
- [2] Mohamed Chahine Bouaziz, Mourad El Koundi, and Ghaleb Ennine. High-resolution solar panel detection in Sfax, Tunisia: A UNet-Based approach. *Renewable Energy*, 235: 121171, 2024. 3
- [3] Kyle Bradbury, Raghav Saboo, Timothy L Johnson, Jordan M Malof, Arjun Devarajan, Wuming Zhang, Leslie M Collins, and Richard G Newell. Distributed solar photovoltaic array location and extent dataset for remote sensing object identification. *Scientific data*, 3(1):160106, 2016. 5
- [4] Lorenzo Brigato and Luca Iocchi. A close look at deep learning with small data. In *2020 25th international conference on pattern recognition (ICPR)*, pages 2490–2497. IEEE, 2021. 2, 3, 6
- [5] Gong Cheng and Junwei Han. A survey on object detection in optical remote sensing images. *ISPRS Journal of Photogrammetry and Remote Sensing*, 117:11–28, 2016. 3
- [6] Gong Cheng, Xingxing Xie, Junwei Han, Lei Guo, and Gui-Song Xia. Remote sensing image scene classification: Benchmark and state of the art. *Proceedings of the IEEE*, 105(10):1865–1883, 2017. 1
- [7] Alexey Dosovitskiy, Lucas Beyer, Alexander Kolesnikov, Dirk Weissenborn, Xiaohua Zhai, Thomas Unterthiner, Mostafa Dehghani, Matthias Minderer, Georg Heigold, Sylvain Gelly, Jakob Uszkoreit, and Neil Houlsby. An Image is Worth 16x16 Words: Transformers for Image Recognition at Scale. In *International Conference on Learning Representations*, 2021. 1
- [8] Nikita Dvornik, Julien Mairal, and Cordelia Schmid. Modeling Visual Context is Key to Augmenting Object Detection Datasets. In *European Conference on Computer Vision*, 2018. 3
- [9] Chelsea Finn, Pieter Abbeel, and Sergey Levine. Model-Agnostic Meta-Learning for Fast Adaptation of Deep Networks. In *Proceedings of the 34th International Conference on Machine Learning*, pages 1126–1135. PMLR, 2017. 3
- [10] Jonathan Frankle and Michael Carbin. The Lottery Ticket Hypothesis: Finding Sparse, Trainable Neural Networks. In *International Conference on Learning Representations*, 2019. 2
- [11] Tyler Furedi, Edwin Kimsal, Samara Cornejo, Nicholas Liero, and Joseph Ranalli. Labeled photovoltaic installations for orthographic aerial imagery in Queens, New York. *Scientific Data*, 2026. 5

- [12] Jordan Hoffmann, Sebastian Borgeaud, Arthur Mensch, Elena Buchatskaya, Trevor Cai, Eliza Rutherford, Diego de Las Casas, Lisa Anne Hendricks, Johannes Welbl, Aidan Clark, Thomas Hennigan, Eric Noland, Katherine Millican, George van den Driessche, Bogdan Damoc, Aurelia Guy, Simon Osindero, Karén Simonyan, Erich Elsen, Oriol Vinyals, Jack Rae, and Laurent Sifre. An empirical analysis of compute-optimal large language model training. In *Advances in Neural Information Processing Systems*, pages 30016–30030. Curran Associates, Inc., 2022. 1, 2, 3, 6
- [13] International Energy Agency. World Energy Outlook 2023, 2023. 1, 3
- [14] Glenn Jocher and Jing Qiu. Ultralytics YOLO11, 2024. 2, 4
- [15] Jared Kaplan, Sam McCandlish, Tom Henighan, Tom B Brown, Benjamin Chess, Rewon Child, Scott Gray, Alec Radford, Jeffrey Wu, and Dario Amodei. Scaling laws for neural language models. *arXiv preprint arXiv:2001.08361*, 2020. 1, 2, 3
- [16] Gabriel Kasmi. *Enhancing the Reliability of Deep Learning Models to Improve the Observability of French Rooftop Photovoltaic Installations*. Theses, Université Paris sciences et lettres, 2024. Issue: 2024UPSLM027. 3
- [17] Gabriel Kasmi, Laurent Dubus, Philippe Blanc, and Yves-Marie Saint-Drenan. Towards Unsupervised Assessment with Open-Source Data of the Accuracy of Deep Learning-Based Distributed PV Mapping. In *Proceedings of the Workshop on Machine Learning for Earth Observation (MACLEAN)*, 2022. in conjunction with ECMLPKDD 2022. 3
- [18] Gabriel Kasmi, Yves-Marie Saint-Drenan, David Trebosc, Raphaël Jolivet, Jonathan Leloux, Babacar Sarr, and Laurent Dubus. A crowdsourced dataset of aerial images with annotated solar photovoltaic arrays and installation metadata. *Scientific Data*, 10(1), 2023. 5
- [19] Gabriel Kasmi, Laurent Dubus, Yves-Marie Saint-Drenan, and Philippe Blanc. Space-scale exploration of the poor reliability of deep learning models: the case of the remote sensing of rooftop photovoltaic systems. *Environmental Data Science*, 4:e22, 2025. 7
- [20] Bala Bhavya Kausika, Diede Nijmeijer, Iris Reimerink, Peter Brouwer, and Vera Liem. GeoAI for Detection of Solar Photovoltaic Installations in the Netherlands. *Energy and AI*, 6:100111, 2021. 3
- [21] Lucas Kruitwagen, KT Story, J Friedrich, L Byers, S Skillman, and Cameron Hepburn. A global inventory of photovoltaic solar energy generating units. *Nature*, 598(7882): 604–610, 2021. 5
- [22] Darius Lam, Richard Kuzma, Kevin McGee, Samuel Doolley, Michael Laielli, Matthew Klaric, Yaroslav Bulatov, and Brendan McCord. xView: Objects in Context in Overhead Imagery, 2018. 6
- [23] Anqi Li, Luling Liu, Shijie Li, Xihong Cui, Xuehong Chen, and Xin Cao. Global photovoltaic solar panel dataset from 2019 to 2022. *Scientific Data*, 12(1):637, 2025. 5
- [24] Tsung-Yi Lin, Michael Maire, Serge Belongie, James Hays, Pietro Perona, Deva Ramanan, Piotr Dollár, and C Lawrence Zitnick. Microsoft COCO: Common Objects in Context. In *European conference on computer vision*, pages 740–755. Springer, 2014. 6
- [25] Tsung-Yi Lin, Piotr Dollar, Ross Girshick, Kaiming He, Bharath Hariharan, and Serge Belongie. Feature Pyramid Networks for Object Detection. In *Proceedings of the IEEE Conference on Computer Vision and Pattern Recognition (CVPR)*, 2017. 3, 5
- [26] Kevin Mayer, Benjamin Rausch, Marie-Louise Arlt, Gunther Gust, Zhecheng Wang, Dirk Neumann, and Ram Rajagopal. 3D-PV-Locator: Large-scale Detection of Rooftop-mounted Photovoltaic Systems in 3D. *Applied Energy*, 310:118469, 2022. 3
- [27] OpenStat Madagascar. Données sur l'énergie solaire et labellisation d'images de panneaux photovoltaïques à Madagascar, 2025. 1, 3, 4
- [28] Alejandro Pardo, Mengmeng Xu, Ali Thabet, Pablo Arbeláez, and Bernard Ghanem. BAOD: budget-aware object detection. In *Proceedings of the IEEE/CVF Conference on Computer Vision and Pattern Recognition*, pages 1247–1256, 2021. 2, 3
- [29] Poonam Parhar, Ryan Sawasaki, Alberto Todeschini, Colorado Reed, Hossein Vahabi, Nathan Nusaputra, and Felipe Vergara. HyperionSolarNet: Solar Panel Detection from Aerial Images. In *NeurIPS 2021 Workshop on Tackling Climate Change with Machine Learning*, 2021. 3
- [30] Jacob Shermeyer and Adam Van Etten. The effects of super-resolution on object detection performance in satellite imagery. In *Proceedings of the IEEE/CVF Conference on Computer Vision and Pattern Recognition Workshops*, pages 0–0, 2019. 2, 3, 8
- [31] Baifeng Shi, Ziyang Wu, Maolin Mao, Xin Wang, and Trevor Darrell. When Do We Not Need Larger Vision Models? In *NeurIPS 2024 Workshop: Self-Supervised Learning - Theory and Practice*, 2024. 2
- [32] Bharat Singh and Larry S. Davis. An Analysis of Scale Invariance in Object Detection - SNIP. *2018 IEEE/CVF Conference on Computer Vision and Pattern Recognition*, pages 3578–3587, 2017. 3
- [33] Bharat Singh, Mahyar Najibi, and Larry S Davis. SNIPER: Efficient Multi-Scale Training. In *Advances in Neural Information Processing Systems*. Curran Associates, Inc., 2018. 3, 8
- [34] Jake Snell, Kevin Swersky, and Richard S. Zemel. Prototypical Networks for Few-shot Learning. In *Neural Information Processing Systems*, 2017. 3
- [35] Mingxing Tan and Quoc Le. Efficientnet: Rethinking model scaling for convolutional neural networks. In *International conference on machine learning*, pages 6105–6114. PMLR, 2019. 2, 4
- [36] Vladimir Vapnik. *The nature of statistical learning theory*. Springer science & business media, 2013. 2, 6
- [37] Gui-Song Xia, Xiang Bai, Jian Ding, Zhen Zhu, Serge Belongie, Jiebo Luo, Mihai Datcu, Marcello Pelillo, and Liangpei Zhang. DOTA: A large-scale dataset for object detection in aerial images. In *Proceedings of the IEEE conference on computer vision and pattern recognition*, pages 3974–3983, 2018. 6

- [38] Jason Yosinski, Jeff Clune, Yoshua Bengio, and Hod Lipson. How transferable are features in deep neural networks? In *Advances in Neural Information Processing Systems*. Curran Associates, Inc., 2014. [3](#)
- [39] Jiafan Yu, Zhecheng Wang, Arun Majumdar, and Ram Rajagopal. DeepSolar: A Machine Learning Framework to Efficiently Construct a Solar Deployment Database in the United States. *Joule*, 2(12):2605–2617, 2018. [3](#)
- [40] Xiaohua Zhai, Alexander Kolesnikov, Neil Houlsby, and Lucas Beyer. Scaling Vision Transformers. In *Proceedings of the IEEE/CVF Conference on Computer Vision and Pattern Recognition (CVPR)*, pages 12104–12113, 2022. [1](#)

Is Bigger Always Better? Efficiency Analysis in Resource-Constrained Small Object Detection

Supplementary Material

7. Additional details on the dataset

Geographic distribution. Figure 7 presents the geographic distribution of the 8,977 drone images retained for our analysis, colored by split assignment. Images are concentrated along major transportation corridors and around Antananarivo, reflecting the crowdsourced collection methodology, with secondary clusters along the east coast and in the southern regions around Fianarantsoa and Toliara. The random split yields a spatially representative test set covering the full geographic extent of the dataset.

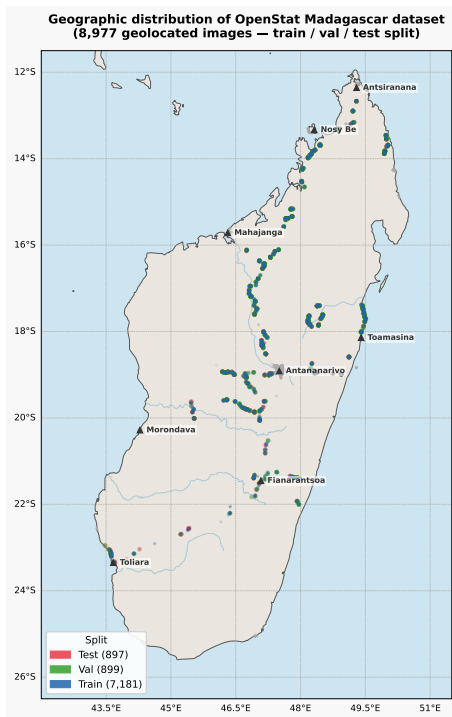


Figure 7. **Geographic distribution of the 8,977 drone images retained for training, colored by split assignment (train / val / test).** Sampling points follow major transportation corridors and population centers, with Antananarivo as the primary cluster. The random split preserves the spatial coverage of the full dataset across all three subsets.

Representative images. Figure 8 shows two representative drone images from the OpenStat Madagascar dataset, illustrating the diversity of rooftop configurations, installation types, and imaging conditions. Individual solar panels are clearly visible but occupy a small fraction of the total

image area, consistent with the bounding box size distribution reported in Figure 2.



Figure 8. **Representative high-resolution drone images from the OpenStat Madagascar dataset.** Images illustrate the variety of rooftop types, panel orientations, and background clutter encountered across acquisition sites.

Annotated examples. Figure 9 shows examples of images with ground-truth bounding box annotations from the validation set. Each box corresponds to an individual solar panel or boiler identified by a human annotator. The high density of small, tightly-packed boxes in some images illustrates the detection difficulty and confirms the small object characterization established in Section 4.



Figure 9. **Validation set images with ground-truth bounding box annotations.** Dense clusters of small boxes are characteristic of rooftop installations with multiple panels, and represent the dominant challenge in this detection task.

8. Additional tables

Experimental coverage. Table 3 presents the 44 configurations completed out of 60 nominal combinations. The 16 excluded configurations correspond to large models at high resolution, which exceed the available GPU memory (NVIDIA A2, 16GB).

Table 3. **Available model configurations per (resolution, dataset fraction) combination.** Missing entries are due to GPU memory constraints (NVIDIA A2, 16GB). A total of 44 training runs were completed.

Resolution	Fraction	N	S	M	L	X
416px	10%	✓	✓	✓	✓	✓
	25%	✓	✓	✓	✓	✓
	50%	✓	✓	✓	✓	✓
	100%	✓	✓	✓	✓	✓
640px	10%	✓	✓	✓	✓	
	25%	✓	✓	✓	✓	
	50%	✓	✓	✓	✓	
	100%	✓	✓	✓	✓	
1280px	10%	✓	✓			
	25%	✓	✓			
	50%	✓	✓			
	100%	✓	✓			

Efficiency statistics. Table 4 reports per-model efficiency statistics (min, max, average) across all completed training configurations, along with the best-performing (dataset

fraction, resolution) pair and its corresponding mAP_{50} . YOLO11N dominates on all three statistics; notably, even its minimum efficiency (1.056) exceeds the maximum efficiency of any other variant.

Table 4. **Efficiency statistics per model variant.** Efficiency is defined as $mAP_{50} / \text{ModelSize (MB)}$. Best Config reports the (dataset fraction, resolution) achieving the highest efficiency, along with the corresponding mAP_{50} .

Model	Min Eff.	Max Eff.	Avg Eff.	Best Config	mAP_{50}
YOLO11-N	1.056	1.176	1.124	10% / 1280 px	0.617
YOLO11-S	0.277	0.329	0.302	25% / 640 px	0.597
YOLO11-M	0.124	0.149	0.137	100% / 640 px	0.573
YOLO11-L	0.096	0.117	0.106	100% / 640 px	0.566
YOLO11-X	0.044	0.049	0.046	100% / 416 px	0.533

9. Additional results

9.1. Consistency Across Efficiency Measures

Table 5 reports average efficiency across all training configurations for each model variant, computed under five alternative performance metrics. YOLO11N achieves the highest efficiency under all measures, and the ranking $N > S > M > L > X$ is perfectly monotonic across all five columns — no metric reversal is observed anywhere in the table. The efficiency gap between YOLO11N and YOLO11X ranges from $20\times$ (mAP_{50} and mAP_{50-95}) to $23\times$ (Precision), confirming that the efficiency inversion reported in Sec. 5.1 is not an artifact of the choice of performance measure but a structural property of the data-scarce regime.

Table 5. **Efficiency under alternative performance metrics.** Each column reports the average efficiency (metric / model size in $\text{MB} \times 10$) across all training configurations. YOLO11-N consistently achieves the highest efficiency regardless of the metric used.

Model	Eff. (mAP_{50})	Eff. (mAP_{50-95})	Eff. (Precision)	Eff. (Recall)	Eff. (F_1)
YOLO11N	1.124	0.835	1.341	1.158	1.242
YOLO11S	0.302	0.220	0.366	0.316	0.339
YOLO11M	0.137	0.098	0.171	0.143	0.155
YOLO11L	0.106	0.076	0.135	0.112	0.123
YOLO11X	0.046	0.032	0.060	0.049	0.054

9.2. Robustness Across Configurations

Table 6 confirms the dominance of YOLO11N under a fair, iso-configuration comparison. Restricting the analysis to 416 px — the only resolution at which all five variants were evaluated — YOLO11N achieves the highest efficiency across all dataset fractions (1.056–1.109), with scores remaining stable regardless of data volume. This rules out the hypothesis that larger models might dominate under specific data regimes: even at 10% of the dataset, YOLO11N outperforms all larger variants while maintaining competitive absolute mAP_{50} (0.548).

Table 6. **Best model per iso-configuration.** Only configurations where all five YOLO11 variants were evaluated are included. YOLO11N dominates across all tested configurations.

Fraction	Resolution	Efficiency	mAP ₅₀
10%	416 px	1.080	0.548
25%	416 px	1.056	0.536
50%	416 px	1.064	0.540
100%	416 px	1.109	0.563

9.3. Zero-Shot Performance

Table 7 reports zero-shot performance of all YOLO11 variants on the OpenStat Madagascar test set using COCO-pretrained weights without fine-tuning. All values are near-zero ($\text{mAP}_{50} \leq 0.004$ across all models and resolutions), confirming the complete absence of exploitable domain transfer from COCO pretraining to rooftop PV detection. Importantly, there is no performance gradient across model sizes — larger pretrained representations confer no advantage, ruling out the hypothesis that richer features compensate for the domain gap.

Table 7. **Zero-shot evaluation of YOLO11 variants on the OpenStat Madagascar test set, averaged across available resolutions.** All values are near-zero (≤ 0.004), confirming the absence of domain transfer from COCO pretraining.

Model	mAP ₅₀	mAP ₅₀₋₉₅	Precision	Recall	F ₁
YOLO11N	0.0022	0.0011	0.0041	0.0422	0.0075
YOLO11S	0.0014	0.0007	0.0027	0.0287	0.0049
YOLO11M	0.0012	0.0005	0.0024	0.0179	0.0042
YOLO11L	0.0010	0.0004	0.0018	0.0096	0.0030
YOLO11X	0.0013	0.0006	0.0024	0.0116	0.0040

9.4. Resolution and Model Size Interaction

Table 8 reports mean mAP₅₀ and efficiency per (model, resolution) cell, averaged across dataset fractions. Two distinct patterns emerge. In absolute mAP₅₀, resolution benefits all models uniformly: YOLO11N improves from 0.547 at 416 px to 0.606 at 1280 px, while the gap between YOLO11N and YOLO11S narrows substantially at 640 px ($\Delta = 0.002$), suggesting that higher resolution partially compensates for the capacity deficit of smaller models in raw detection performance. In efficiency, however, the ratio between YOLO11N and YOLO11S remains stable at $\approx 3.7\times$ across all three resolution levels (1.08 vs. 0.29 at 416 px; 1.15 vs. 0.32 at 640 px; 1.15 vs. 0.30 at 1280 px): resolution scales efficiency proportionally without altering the relative ranking. Resolution and model size thus operate on orthogonal axes — resolution is a universal performance lever, but does not compensate for the overparameterization penalty when deployment cost is accounted for.

Table 8. **Resolution–model size interaction.** Mean mAP₅₀ (upper block) and mean efficiency (mAP₅₀ / 10 MB, lower block) per (model, resolution) cell, averaged across dataset fractions. Bold denotes the best value per column. N/A: excluded due to memory constraints. The efficiency ratio YOLO11N/YOLO11S remains $\approx 3.7\times$ at all resolutions.

	Resolution	YOLO11N	YOLO11S	YOLO11M	YOLO11L	YOLO11X
mAP ₅₀	416 px	0.547	0.518	0.509	0.500	0.499
	640 px	0.584	0.578	0.542	0.530	N/A
	1280 px	0.600	0.556	N/A	N/A	N/A
Efficiency	416 px	1.08	0.29	0.13	0.10	0.05
	640 px	1.15	0.32	0.14	0.11	N/A
	1280 px	1.14	0.30	N/A	N/A	N/A